Article
Optimal Design of a Single-Phase Bidirectional Rectifier

Vicente Esteve [1,*] **, Juan L. Bellido** [1,2] **and José Jordán** [1]

1   Department of Electronic Engineering, University of Valencia, 46100 Valencia, Spain;
     jbellido@sictechinduction.com (J.L.B.); jose.jordan@uv.es (J.J.)
2   R&D Department, SiCtech Induction, 46980 Paterna, Spain
*   Correspondence: vesteveg@uv.es

Abstract: This article outlines the comprehensive design and control approach for a single-phase bidirectional rectifier (SPBR) used in bidirectional charging of electric vehicle batteries. The operational parameters of the inverter are determined through a thorough analysis of all switching sequences to accurately assess power losses, considering the type of switching device chosen in each case, enabling proper component sizing, and understanding converter efficiency. An exclusive electronic control circuit is examined, governing two converter operation modes: boost rectifier with power factor correction (PFC) and sine pulse inverter width modulation (SPWM) with a minimum number of adjustments made automatically. One problem that arises when addressing the design of an SPBR is determining the operating frequency. To address this issue, this study offers to conduct a comparative analysis of losses using various power devices and magnetic circuits to determine the optimal operating frequency for achieving maximum energy efficiency. To validate the design's feasibility, a prototype with 10 kW output power was constructed, achieving a peak efficiency of approximately 97.5% in both directions, unity power factor (PF), and total harmonic distortion (THD) of less than 7% during full power operation.

Keywords: index terms; power conversion; bidirectional converters; boost rectifier with power factor correction; SPWM inverters; efficiency

1. Introduction

A successful transition to sustainable energy requires innovative strategies and meticulous planning to effectively integrate emerging technologies and devices for electricity production and storage. This concept is often referred to as "smart electrification" by various authors [1]. Electric vehicles (EVs) are playing a significant role in this transition. When EVs are parked and connected to charging stations, they can contribute power to the grid or the owner's home during peak demand periods, a concept known as vehicle-to-grid (V2G) or vehicle-to-home (V2H) strategies. Moreover, the energy stored in EV batteries can be utilized to stabilize voltage and frequency fluctuations on the grid. To enable these functionalities, converters linking the grid to EVs must facilitate bidirectional energy flow [2].

Figure 1 depicts a diagram illustrating the described solution for a single-phase 230 V AC mains supply scenario [3]. The SPBR (single-phase bidirectional rectifier) block connects to the power grid via an inductance. The BDC (bidirectional DC-DC converter) block links the EV battery to the DC-link capacitor. Through the electronic control of the complete converter, the amplitude and direction of current I_2 can be regulated for the specified values of SPBR output voltage V_1 and nominal battery voltage V_2. In a conventional battery charging process, current I_2 moves from the network to the battery. Conversely, when the battery's energy is utilized to supply power to the grid, the direction of I_2 is reversed [4]. Furthermore, integrating renewable energy systems and bidirectional EV chargers facilitates smart electrification and reduces network operating costs by providing grid support and leveraging the EV battery as a power reserve [5].
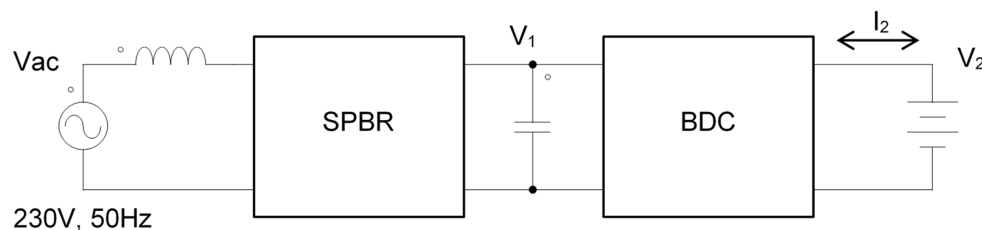
Figure 1. Block diagram of a V2G(H) converter.

The most immediate solution for the BDC involves a basic bidirectional DC-DC converter [6]. However, for safety purposes, this converter must incorporate galvanic isolation. These converters are known as isolated bidirectional DC-DC converters (IBDC). A widely accepted solution involves using a converter that utilizes either two full bridges of transistors dual active bridges DAB (dual active bridges DAB) [7] or two half-bridges (dual active half-bridges DAHB) [8] connected in a configuration where the output of one serves as the input of the other. For high power levels, this topology can be further optimized by employing multiphase DAB [9].

The typical topology for the SPBR block comprises a conventional transistorized single-phase full-bridge boost rectifier with pulse-width modulation controlled by the input current and the output voltage, operating at unity power factor and possessing power reversal capability [10,11]. In the case of three-phase mains, the preferred solution adopted is based on full bridges with three transistor legs [12,13].

Until now, several pulse width modulation (PWM) strategies have been utilized in a single-phase AC-DC converter such a bipolar (BPWM), unipolar (UPWM) [14,15], hybrid modulation (HPWM) [16], and hysteresis current control (HCC) [17]. In order to reduce power losses and electromagnetic interferences (EMI), soft switching modulation [18] and resonant rectifiers [19] have been presented that can include galvanic isolation [20].

In recent years, significant research efforts have been directed towards enhancing the efficiency of these converters, especially concerning bidirectional power flow. While many existing studies have proposed solutions for bidirectional power conversion, a research gap persists regarding the criteria for selecting the optimal operating frequency to enhance efficiency and ensure bidirectional power flow in single-phase systems.

Another important objective of this paper is to explore the possibility of optimizing the efficiency of the converter. Several design parameters play a role in enhancing efficiency, including the selection of power devices, operating frequency, and the design of magnetic components [21–23].

This paper introduces a comprehensive design and control methodology for a single-phase bidirectional rectifier (SPBR) applied to the bidirectional charging of electric vehicle batteries. A thorough analysis of all switching sequences has been conducted to define the operating conditions of the converter accurately. This analysis enables the precise determination of all power losses, facilitating proper component sizing and understanding of converter efficiency. Additionally, a fully operational control circuit, easily implementable on the PSIM simulator, has been presented. This circuit allows the verification of the correct operation of the converter and serves as the foundation for the control system that is ultimately implemented on an FPGA-based system. Furthermore, a comparative analysis of losses is performed using various power devices and magnetic circuits to ascertain the optimal operating frequency for achieving the maximum energy efficiency.

In summary, this paper aims to fill a research gap by presenting a novel approach for the design and control of SPBRs, offering an improved method for determining the optimal operating frequency of SPBR converters for bidirectional power conversion applications in modern single-phase power systems.

The paper is structured as follows: Section 2 focuses on the configuration of the SPBR converter. In Section 3, an analysis of the SPBR converter is conducted, followed by analysis of power loss and efficiency of the converter in Section 4. In Section 5, the proposed SPBR

control method is introduced. Section 6 presents the comparative analysis that permits to determinate de optimal operating frequency. The validation of results using experimental data is presented in Section 7. Finally, the conclusions are drawn.

2. SPBR Configuration

Figure 2 shows the simplified configuration of the SPBR. The converter consists of a full bridge with four switches connected to the single-phase grid via inductors, which are used to filter the grid current. In order to provide bidirectional current flow, transistors can conduct positive and negative currents. Electrolytic capacitor is used for voltage filtering at the DC side of the inverter.
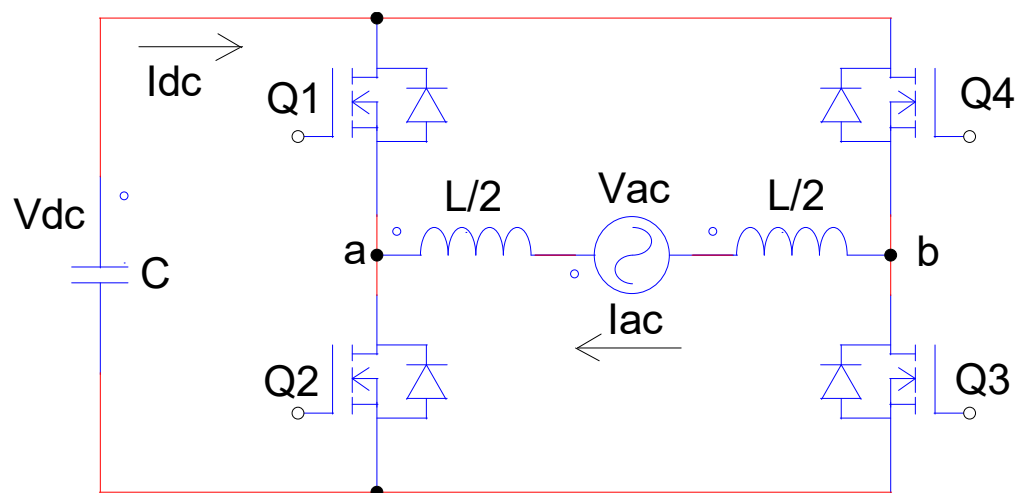

Figure 2. SPBR configuration.

Since the converter is bidirectional, it has two modes of operation. When power flows from the DC side to the AC side, the converter acts as a voltage source inverter (VSI); however, when power is drawn from the mains, the converter acts as a PFC active boost rectifier. By the means of the SPWM technique, switching signals are obtained by comparing a sinusoidal voltage with a triangle wave, obtaining on the AC side of the converter a PF near the unit with low THD. Using a UPWM control technique, the effective switching frequency is doubled and that results in a smaller ripple in the DC side current and a significantly lower harmonic content on the AC side compared to the BPWM [14].

The design has been made for a fast bidirectional charging application of lithium-ion EV batteries using a typical conventional charging process [24]. Table 1 shows several values that serve as specifications for the converter design.

Table 1. SPBR specifications.

Specification	Symbol	Value	Unit
Maximum Power	P	10	kW
Mains Voltage	V_{AC}	230	V
Mains Frequency	f	50	Hz
Regulated DC Voltage	V_{DC}	385	V
Power Factor	PF	1	
Total Harmonic Distortion	THD	7	%
Mains Current Ripple	ΔI_{AC}	5	A
DC Voltage Ripple	ΔV_{DC}	5	V
Efficiency	η	97.5	%

For this application, the standardized values of the European single-phase electrical network have been chosen. The choice of the DC voltage value has been selected as a typical value that allows for proper regulation without penalizing efficiency. The network quality values, ripples, and efficiency are typical objective values for the application. The operating frequency of the converter has not been specified since it will be determined as a result of the comparative study conducted in Section 6.

3. Analysis of the SPBR

The main design equations of the converter, valid for both inverter and rectifier operations, have been presented in well-known technical manuals and application notes [15,25]. The conduction cycle of the SPWM modulation varies proportionally with the amplitude of the mains voltage and its maximum value is calculated as follows:

$$D_{\max} = \frac{\eta V_{AC} \sqrt{2}}{V_{DC}}. \tag{1}$$

The total line inductance filter was obtained with the following equation:

$$L = \frac{(1 - D_{\max}) V_{AC}}{2\sqrt{2} f_S \Delta I_{AC}} \tag{2}$$

and the capacitance of the *DC* side filter is calculated as follows:

$$C = \frac{\eta P}{4\pi f V_{DC} \Delta V_{DC}}. \tag{3}$$

The *AC* and *DC* currents are obtained with the following equations:

$$I_{ACrms} = \frac{P}{\eta \, PF \, V_{AC}}, \tag{4}$$

$$I_{DC} = \frac{\eta P}{V_{DC}}. \tag{5}$$

Figure 3 shows the switching sequence of a complete period of the SPBR operating in rectifier mode. This figure is organized in four two columns for positive (left) and negative (right) mains voltage cycle. The top of each column shows the waveforms of the four gate trigger signals V_{G1}, V_{G2}, V_{G3}, and V_{G4} of the transistors and the current I_{AC} in the inductor. The switching sequence steps are identified by numbers, and the corresponding inverter schematics for each step are presented below. The current-carrying devices are drawn with solid lines, and the voltage-blocking devices are drawn with dotted lines. The direction of the current and the polarity of the voltage obtained at the end of each step have been expressed using arrows and ±signs. The capacitors $C_1 \ldots C_4$ represent the output capacitance of the transistors. To simplify the diagrams, only one inductor has been drawn.

In the rectifier mode, current normally flows from the AC side to the DC side through the transistors in reverse mode while they are active. This occurs in time intervals ①, ④, ⑦, and ⑩. When the high-side and low-side MOSFETs of a vertical arm of the bridge are turned-on simultaneously, a short circuit occurs between the V_{DC} and its ground, generating a very large current spike. A period of dead time is provided for turning-off both MOSFETs to prevent such current spikes from occurring, while the inductor current continues to flow. During the dead time, this inductor current flows to the body diode on the opposite side of MOSFET until the corresponding parallel transistor is activated. This occurs in the intervals ②, ⑥, ⑧, and ⑫. For a correct visualization of the different driving states, the dead times are shown to be exaggerated with respect to the cycle period.

The first line of numbers in the waveform header marks the switching transitions. Time intervals ⑤ and ⑪ are relatively soft transitions controlled by the inductor current, while ③ and ⑨ are hard switching where the reverse recovery current of the diode occurs. In time intervals ④ and ⑩, the inductance is charged, and only the DC capacitor feeds the load. In the rest of time intervals, the current flows directly from the mains to the load.
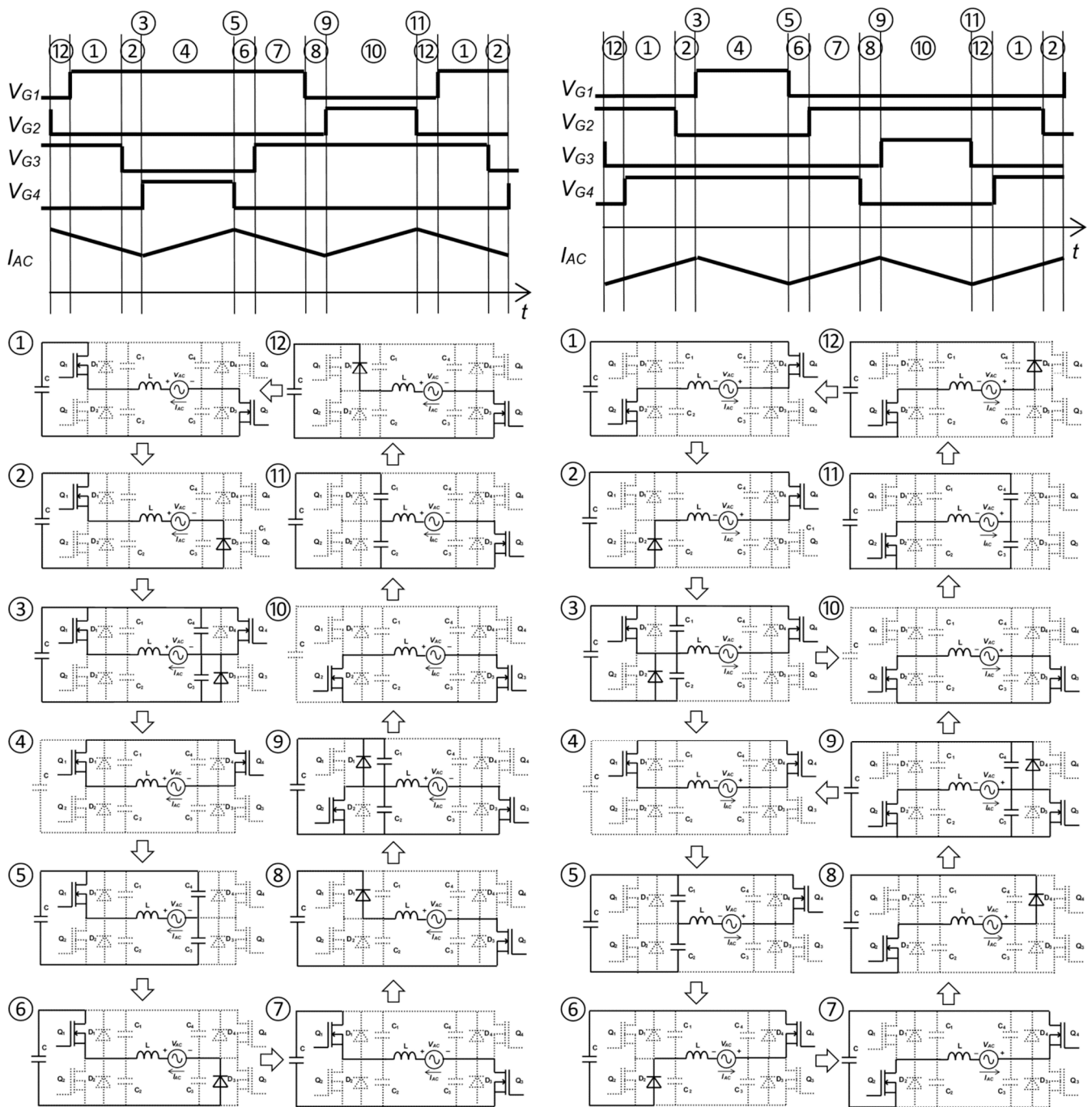
Figure 3. Switching sequence in rectifier mode.

Figure 4 shows the switching sequence of a complete period of the SPBR operating in inverter mode. Now, the conduction of the transistors is direct in time intervals ①, ④, ⑦, and ⑩, allowing the flow of the current from the DC side to the mains. Direct diode conduction occurs in the dead times ③, ⑤, ⑨, and ⑪ and the recovery process occurs in ⑥ and ⑫.

Notably, in both operation modes, when employing IGBT transistors, the reverse current from the switching device must pass through the free-wheeling diode. Consequently, the sequence will be simplified by removing the intervals during which the transistor channel is utilized for reverse currents. Also, the frequency of the inductor current is twice the switching frequency.
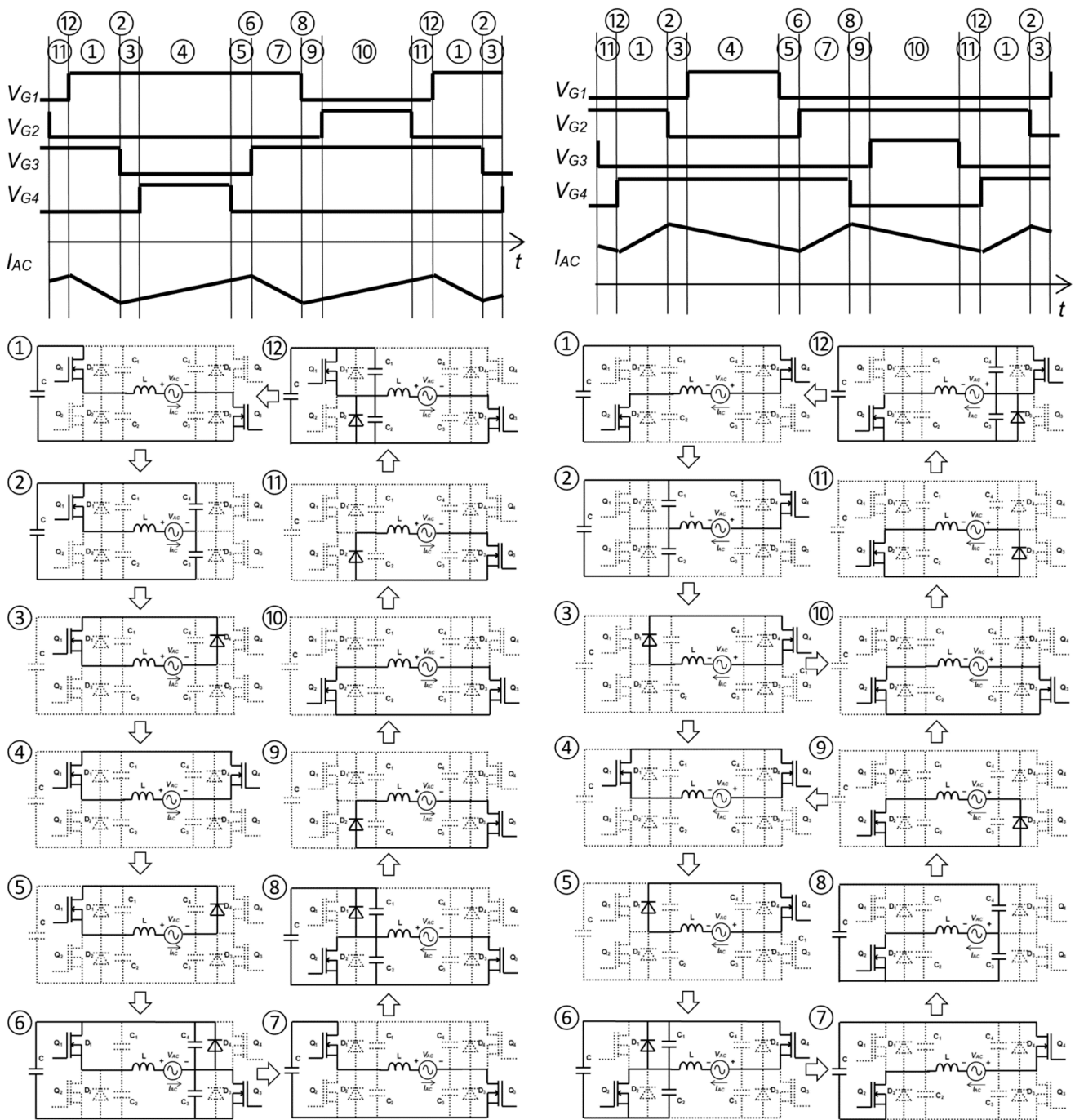
Figure 4. Switching sequence in inverter mode.

4. Power Loss Analysis

A power loss analysis of the SPBR has been carried out considering all the contribution of conduction and switching losses of the transistors including losses from inductances and capacitors. Other losses have not been considered in this study.

In order to calculate the conduction power loss of the transistors P_{QC}, two different cases must be considered. For SiC MOSFET and GaN transistors, it is calculated with the following equation:

$$P_{QC} = I_{Qrms}{}^2 R_{DSon} \tag{6}$$

where I_{Qrms} is the root means square (rms) value of the current through the transistor that is calculated with the following equation:

$$I_{Qrms} = \sqrt{\frac{I_{ACrms}^2}{2} + \frac{\Delta I_{AC}^2}{6}}. \tag{7}$$

However, for IGBTs, the conduction loss analysis must take into account that the positive current flows through the transistor, while the negative current flows through the diode according to the next equation:

$$P_{QC} = I_{Trms}^2 r_T + I_{Tavg} V_{CE(sat)} + I_{Drms}^2 r_D + I_{Davg} V_F \tag{8}$$

where I_{Trms} and I_{Tavg} are the rms and average values of the transistor direct current, and I_{Drms} and I_{Davg} are the rms and average values of the free-wheeling diode. The loss model of the transistor and diodes is given by the parameters $V_{CE(sat)}$, r_T, V_F, and r_D that can be extracted from the manufacturer's data.

The switching power loss of the transistor must consider both turn-on and turn-off switching losses using the next equation:

$$P_{QS} = (E_{OFF} + E_{ON})f \tag{9}$$

where E_{ON} and E_{OFF} are, respectively, the accumulated switching ON and OFF energies in a mains cycle. E_{OFF} is calculated using the graphs provided by the manufacturer using the following polynomial function [26].

$$E_{OFF} = \sum_{i=0}^{f_S/2f} a(I_S(i) + \Delta I_{AC})^2 + b(I_S(i) + \Delta I_{AC}) + c \tag{10}$$

where a, b, and c take values given by manufactures, and $I_S(i)$ is the transistor current in the different turn-off transitions:

$$I_S(i) = \sqrt{2}I_{AC} \sin\left(2\pi \frac{f}{f_S} i\right). \tag{11}$$

Analogously, the accumulated switching energy in turn-on can be calculate with the following equation:

$$E_{ON} = \sum_{i=0}^{f_S/2f} d(I_S(i) - \Delta I_{AC})^2 + e(I_S(i) - \Delta I_{AC}) + g \tag{12}$$

Finally, the total power loss of each converter transistor is given by the following equation:

$$P_Q = P_{QC} + P_{QS}. \tag{13}$$

Although several losses are generated in the capacitor, including series resistance, leakage, and dielectric loss, these losses are simplified by considering the equivalent series resistance *ERS* and calculating the total capacitor loss with the following equation:

$$P_{CR} = I_{Crms}^2 ESR \tag{14}$$

where I_{Crms} is the rms value of the capacitor currents given by the following equation:

$$I_{Crms} = \frac{P}{\eta} \sqrt{\frac{8\sqrt{2}}{3\pi V_{AC} V_{DC}} - \frac{1}{V_{DC}^2}}. \tag{15}$$

Since the inductor conduction loss is generated by the *DC* resistance (*DCR*) of the winding that forms the inductor, the corresponding power loss is calculated as follows:

$$P_{LR} = \left(I_{ACrms}^2 + 2\Delta I_{AC}^2\right) DCR. \tag{16}$$

The calculation of the core loss is too complex, but it can be approximated using the equation of Steinmetz:

$$P_{LC} = K(2f_S)^\alpha \Delta B^\beta V_e \tag{17}$$

where the specific parameters K, α, and β, and the magnetic material effective volume V are given by the provider of the magnetic core. ΔB can be rewritten in terms of inductance by considering Faraday's equation and its effect on inductor current. Assuming a small variation in L, the inductor current change given in the next equation can be used.

$$\Delta B = \frac{L\,\Delta I_{AC}}{N\,A_e} \tag{18}$$

where A_e is the magnetic material effective area.

Therefore, the total power loss of the converter operating in any mode is given by the following equation:

$$P_{TOT} = 8P_Q + P_{CR} + 2(P_{LR} + P_{LC}). \tag{19}$$

where two transistors are in parallel for each bridge switch.

Consequently, the efficiency is given by the following equation:

$$\eta = 1 - \frac{P_{TOT}}{P}. \tag{20}$$

Once the power losses are known, the thermal design of the transistors can be carried out. Considering the thermal design data in Table 3, the maximum temperature of the transistor junction can be determined using the following equation:

$$T_J = T_A + P_Q(R_{thJC} + R_{thCH}) + 8P_Q R_{thHA}. \tag{21}$$

5. Converter Control

The simplified control scheme of the proposed SPBR is depicted in Figure 5, consisting of a unipolar modulation technique. UPWM typically requires two sinusoidal modulating waves, *Vsin* and its inverter, which have the same magnitude and frequency but are 180 degrees out of phase. These two modulating waves are compared in the block "SPWM Modulator" with a common triangular carrier wave, operating at the switching frequency fs, and generating two gating signals, V_{G1} and V_{G4}, for the upper two switches Q_1 and Q_4 and its complementary signals V_{G2} and V_{G3} for the other two lower switches Q_2 and Q_3. It is important to note that the upper two devices do not switch simultaneously, distinguishing them from BPWM where all four devices switch at the same time. The inverter output voltage V_{ab} (Figure 2) switches between either zero and $+V_{DC}$ during the positive half cycle or zero and $-V_{DC}$ during the negative half cycle of the fundamental frequency; hence, this scheme is called unipolar modulation.

Vsin is generated by the block "Phase Regulator" that modifies the phase of a voltage reference obtained from the network voltage so that the phase between the current and the voltage in the AC side of the converter is zero. This phase is measured by the block "Phase Detector". The amplitude of this reference is modified by the block "Amplitude Regulator" where the output of the DC voltage regulator is selected if the converter operates in the rectifier mode, or the output of the DC current regulator is selected if it operates in the inverter mode.

The unipolar switched inverter offers reduced switching losses and generates less EMI. From an efficiency standpoint, it appears that the unipolar switched inverter has an advantage. This scheme effectively doubles the switching frequency as far as the output harmonics are concerned, compared to the bipolar-switching scheme that reduces the amplitude of the high-frequency current ripple.

As the SPBR acts as a boost converter when operating in the rectified mode, the control system itself cannot limit the capacitor charging current until its voltage reaches the peak value of the grid voltage; therefore, a "Soft Start" auxiliary current control circuit must be used.
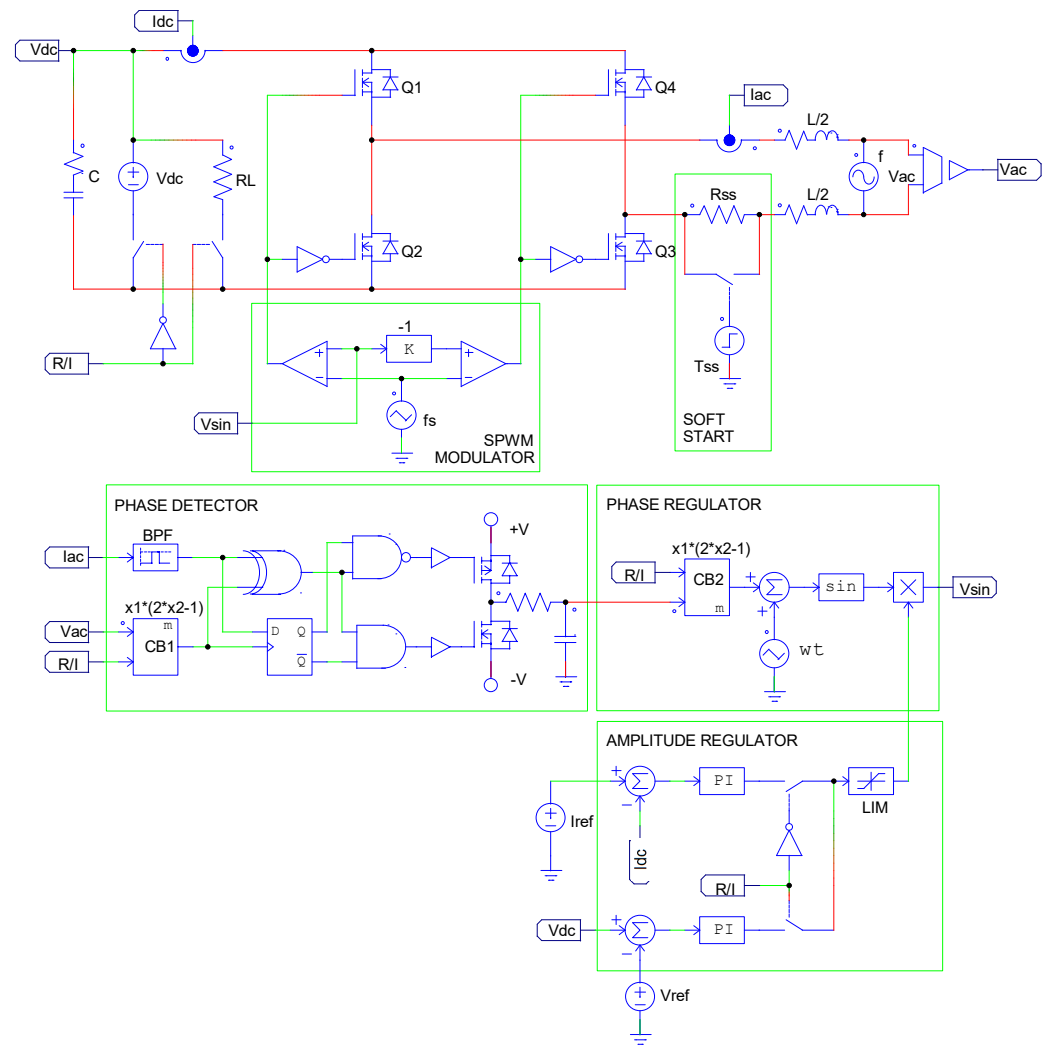
Figure 5. Schematic of the SPBR control.

Given that the circuit must be bidirectional, the converter control should be able to operate in both rectifier and inverter modes with minimal changes, preferably automatically. For this purpose, the signal R/I automatically configures the control for use in the rectifier (R/I = H) or the inverter (R/I = L) mode by changing the polarity of the reference signal in the "Phase Detector" and the "Phase Regulator" and swapping the current and voltage feedback on the DC side for the "Amplitude Regulation" circuit block. Notably, to simplify this control circuit, the generation of dead times has not been considered.

6. Comparative Analysis

In this Section, an analysis of converter losses will be conducted, taking into account the choice of three different switch device technologies. The optimal design depends primarily on the choice of operating frequency, which determines the losses of the power stage and the inductors. In the practical implementation of the converter, the complete bridge is formed by four switches with two transistors of 650 V in parallel to each other. Table 2 shows the main characteristics of the chosen devices for this comparative study.

Table 2. Devices of the power stage.

Symbol	Parameter	Value	Unit
Si IGBT FGH75T65SHDTL4			
$V_{CE(sat)}$	Collector to emitter sat. voltage	1.2	V
r_T	Transistor forward resistance	6	mΩ
V_F	Diode forward voltage	0.9	V
r_D	Diode forward resistance	17	mΩ
$R_{thJC\ trans.}$	Thermal resist. junction-case	0.33	K/W
$R_{thJC\ diode}$	Thermal resist. junction-case	0.65	K/W
R_{thCH}	Thermal resist. case-heatsink	0.3	K/W
SiC MOSFET C3M0060065K			
$R_{DS(on)}$	Drain-source on-state resistance	60	mΩ
a	E_{OFF} first coefficient	10	nJ/A^2
b	E_{OFF} second coefficient	−190	nJ/A
c	E_{OFF} constant term	6.75	μJ
d	E_{ON} first coefficient	40	nJ/A^2
e	E_{ON} second coefficient	1.8	μJ/A
g	E_{ON} constant term	39	μJ
R_{thJC}	Thermal resist. junction-case	0.99	K/W
R_{thCH}	Thermal resist. case-heatsink	0.3	K/W
GaN Transistor GS66508T			
$R_{DS(on)}$	Drain-source on-state resistance	50	mΩ
a	E_{OFF} first coefficient	0	nJ/A^2
b	E_{OFF} second coefficient	233	nJ/A
c	E_{OFF} constant term	0	μJ
d	E_{ON} first coefficient	17.6	nJ/A^2
e	E_{ON} second coefficient	1.59	μJ/A
g	E_{ON} constant term	24.1	μJ
R_{thJC}	Thermal resist. junction-case	0.5	K/W
R_{thCH}	Thermal resist. case-heatsink	0.5	K/W
C	**DC Capacitor**	8.5	mF
ESR	Capacitor equivalent series res.	30	mΩ
I_{Crms}	Capacitor current (rms)	26.8	A
P_{RC}	Total capacitor loss	22.1	W
Heatsink LAM 6 100			
R_{thJA}	Thermal resist. heatsink-ambient	0.2	K/W
T_A	Ambient temperature	40	°C

With all these data, total semiconductors power losses can be calculated using (13).

The design of the inductor also depends on the operating frequency. Its value is determined by (2), and the choice of the number of turns and the magnetic material also depends on the frequency. The construction of the magnetic core will be performed by stacking the several pieces of the KOOL MU 0077192A7 toroidal core. The winding of the inductor will be made with AWG 7 copper cable. A maximum winding factor of 45%

has been chosen, which determines that the maximum number of turns of the inductor is 21. To design the number of core pieces to be stacked, we must set the maximum magnetic flux density to approximately half of its maximum value of 1T that is given by the following equation:

$$B = \frac{L \cdot I_{ACrms}}{\sqrt{2}N \cdot NC \cdot A_e} + \Delta B \tag{22}$$

where L is total inductance calculated in (2), and A_e is the effective magnetic area of each toroidal piece that composed del core. N and NC are the winding turn numbers and the number of stacked cores of each individual inductance. N is calculated with the following equation:

$$N = \sqrt{\frac{L}{2NC \cdot A_L}} \tag{23}$$

where A_L is the effective inductance per square turn of each toroidal core piece. Table 3 shows the main data that allow the designing of the magnetic components.

Table 3. Inductor design parameters (each core piece).

Symbol	Parameter	Value	Unit
I_{ACrms}	Inductor current (rms)	44.6	A
A_e	Core cross effective section	229	mm^2
K	Parameter for core loss density	1.055	
α	Parameter for core loss density	1.988	
β	Parameter for core loss density	33.1	
V_e	Core effective volume	28,600	mm^3
A_L	Effective inductance per square turn	85	nH/T^2

Figure 6 shows the results of the magnetic design in front of bridge-operating frequency. Notably, these curves exhibit discontinuous behavior since both the number of turns and the magnetic flux density are limited. This results in the need to stack an additional toroidal piece in the core when these limits are reached, leading to N and B values that do not correspond to monotonic functions.
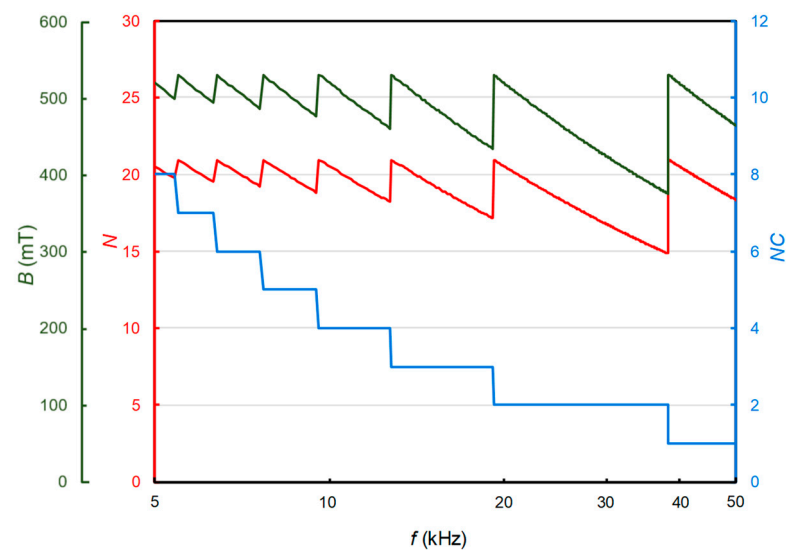

Figure 6. Inductor turns N (red), magnetic flux density B (green), and number of staked cores NC (blue) in front of bridge-operating frequency.

Once the core of each inductance is defined, its power loss can be calculated using (17), introducing the total core volume $NC \cdot V_e$.

To calculate the power losses of the winding, (16) will be used considering that the resistance of AWG 7 wire is 1.63 mΩ per meter, and the total length of the winding is determined by the number of turns and the final geometry of the core.

Taking into account Equations (19) and (20), it is possible to construct the graph of Figure 7 that shows the results obtained for the total power losses and the efficiency of the converter for the three types of devices used as a function of the bridge-operating frequency.
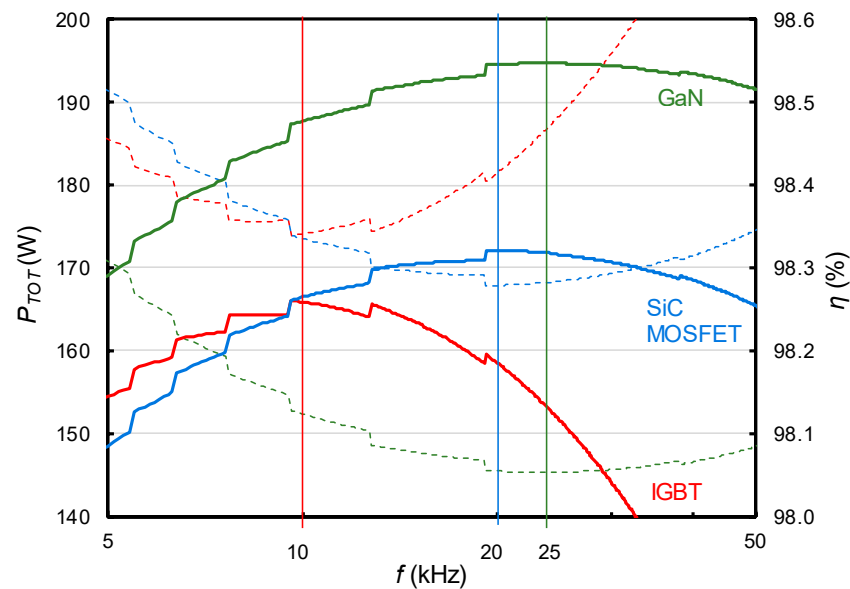

Figure 7. Total power losses (dashed lines) and efficiency (solid lines) of the converter using Si IGBT (red), SiC MOSFET (blue), and GaN transistors (green) in front of bridge-operating frequency.

This graph allows us to find the optimal operating frequency where the maximum efficiency is achieved for each case. It is observed that, with IGBT, the optimal frequency is approximately 10 kHz, with SiC MOSFET, it is 20 kHz, and with GaN transistors, it is 25 kHz. The highest efficiency would be achieved using GaN transistors, with which an efficiency of 98.54% would be achieved. For both SiC MOSFET and GaN converters, the inductors are constructed with a stack of two pieces, while for the IGBT converter, each inductor has four pieces, resulting in the doubling of the volume and mass. Table 4 shows a summary of the results obtained in this study.

Table 4. Summary of the results.

Symbol	Parameter	Value	Unit
Si IGBT FGH75T65SHDTL4			
Optimal f	Operating optimal frequency	10	kHz
L	Inductor value	2×144	μH
P_{QC} *trans.*	Transistor cond. losses (each)	3.3	W
P_{QC} *diode.*	Diode cond. losses (each)	10.1	W
P_{QS}	Switching losses (each)	2.1	W
P_Q *total.*	Bridge total losses	124	W
P_{LR}	Inductor L/2 conduction loss	13.1	W
P_{LC}	Inductor L/2 core loss	0.8	W
P_{TOT}	Total converter losses	174	W
T_J	Junction temperature	91	°C

Table 4. *Cont.*

Symbol	Parameter	Value	Unit
	SiC MOSFET C3M0060065K		
Optimal f	Operating optimal frequency	20	kHz
L	Inductor value	2×72	µH
P_{QC}.	Conduction losses (each)	15	W
P_{QS}	Switching losses (each)	1.0	W
P_Q total.	Bridge total losses	128	W
P_{LR}	Inductor L/2 conduction loss	8	W
P_{LC}	Inductor L/2 core loss	1.1	W
P_{TOT}	Total converter losses	168	W
T_J	Junction temperature	100	°C
	GaN Transistor GS66508T		
Optimal f	Operating optimal frequency	25	kHz
L	Inductor value	2×57	µH
P_{QC}.	Conduction losses (each)	12.5	W
P_{QS}	Switching losses (each)	0.8	W
P_Q total.	Bridge total losses	106	W
P_{LR}	Inductor L/2 conduction loss	7.2	W
P_{LC}	Inductor L/2 core loss	1.3	W
P_{TOT}	Total converter losses	145	W
T_J	Junction temperature	87	°C

7. Experimental Results

This Section shows the experimental results obtained by testing a 10 kW SPBR converter operating according to the specifications shown in Table 1. The values of the components of the circuit are those obtained in the previous Sections. For the experimental verification, a test bed was constructed, consisting of the following elements:

A. A full bridge with eight C3M0060065K SiC MOSFETs with a FPGA-based control mounted on a heatsink.
B. An AC side inductor composed of two pieces of 72 µH.
C. A DC capacitor made of 22 pieces of 390 µF in parallel.
D. Regenerative Bidirectional Programmable DC Power Supply.
E. Mains (230 V, 50 Hz).
F. Digital Storage Oscilloscope (DSO) and probes.
G. Power Analyzer.

The DC side is connected to the IT6012C-800-50 bidirectional laboratory power supply that acts like an electronic load in the rectifier mode or like a voltage supply in the inverter mode. The AC side is connected to the mains. Figure 8 shows a picture of the test bed used to obtain the following experimental results.

Figure 9 shows the experimental measurements of the efficiency in the inverter mode and the rectifier mode regulating power up to 10 kW. The results obtained in both operation modes were very similar. Notably, there are some differences between the experimental and calculated results that may be due to the modeling method used and the existence of losses of other elements not taken into account in the calculation (conductors, connections, parasitic components, voltage and current sensors, etc.) and also due to the measurement process.
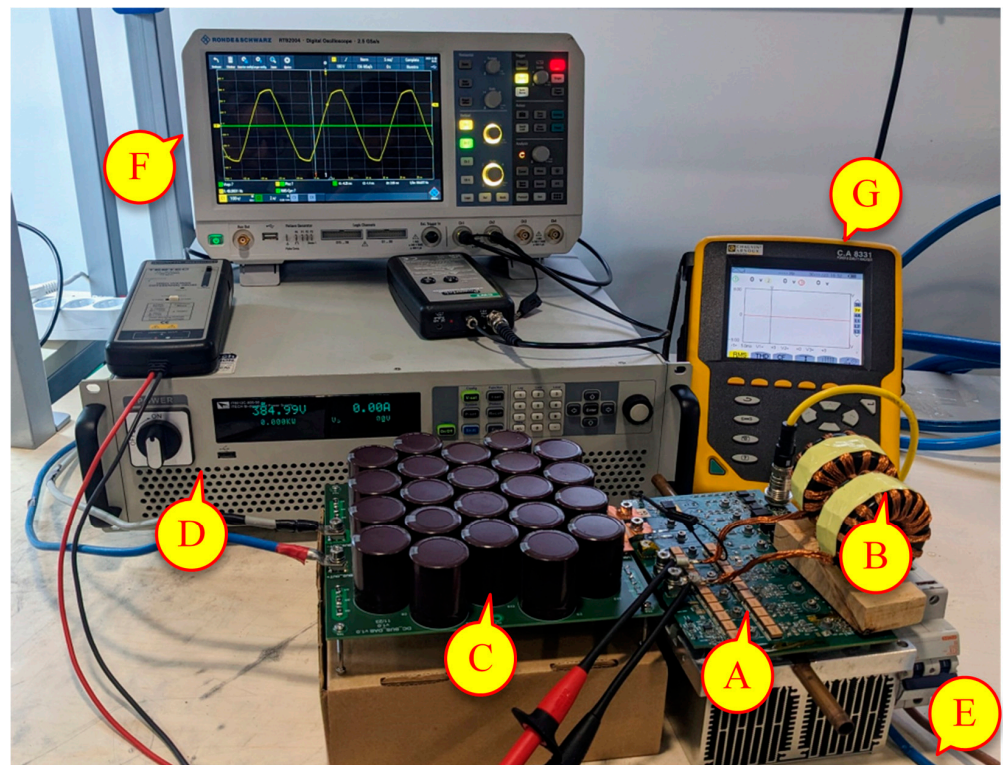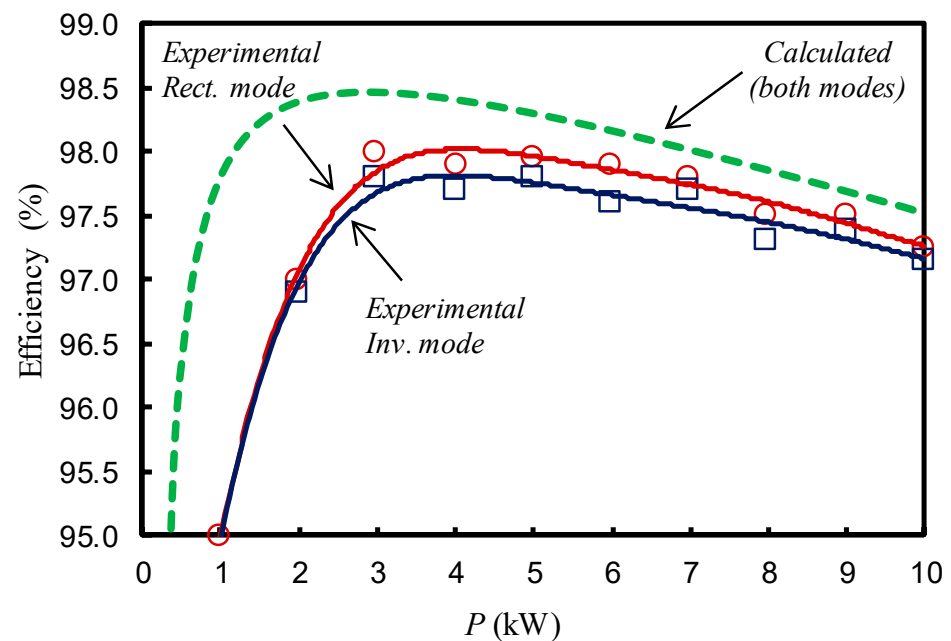
Figure 8. SPBR test bed.

Figure 9. Calculated and experimental efficiency of SPBR converter functioning on the AC active power in the rectifier mode and the DC power in the inverter mode. Solid lines and marking symbols represent the experimental measurements. Dashed lines represent calculated predictions.

Finally, Figure 10 display waveforms captured by digital oscilloscope for the SPBR converter operating in the rectifier and inverter modes at full power with 385 V on the DC side and 230 V_{rms} on the AC side. The switching frequency is 20 kHz. The measured power factor was 1.0, and the THD was less than 7%.
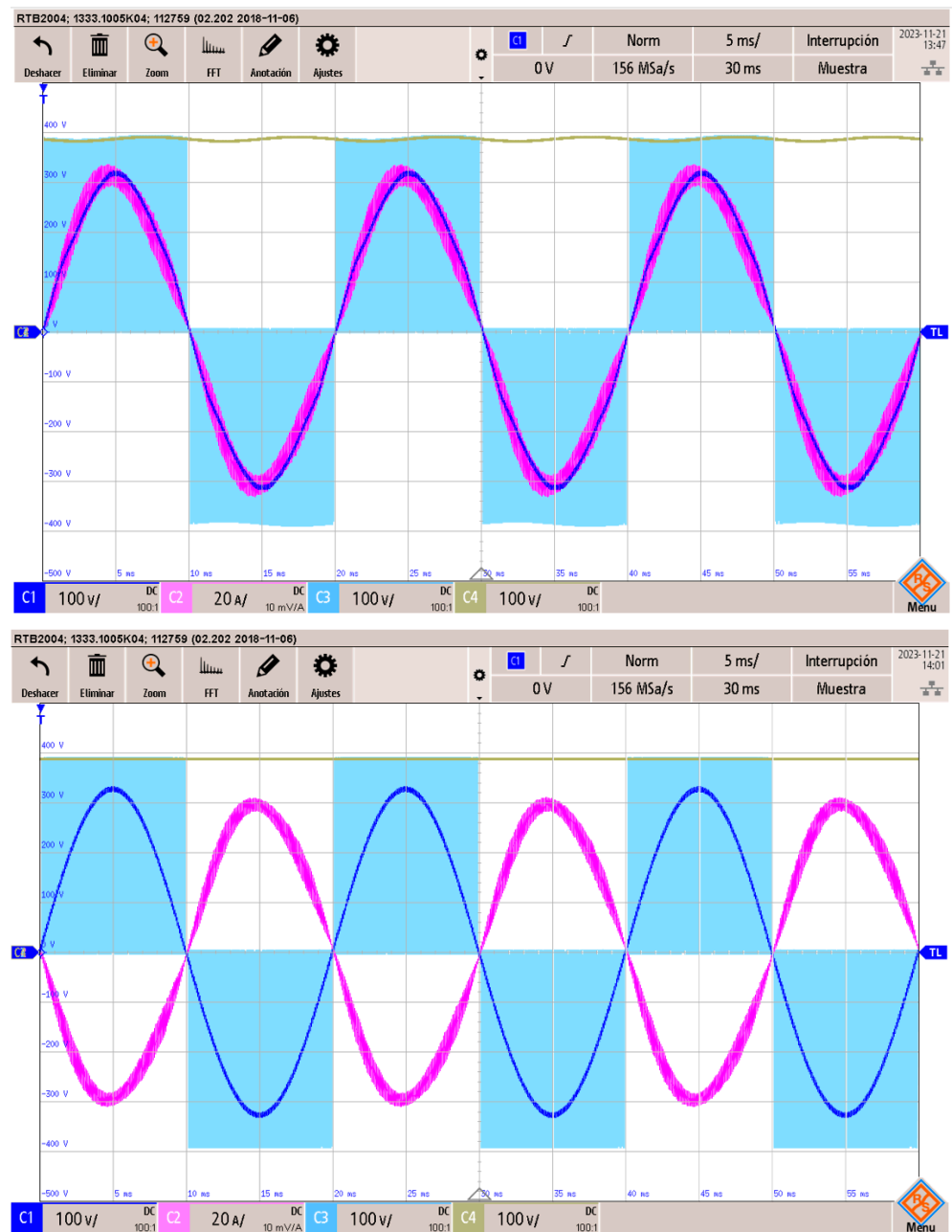
Figure 10. Experimental waveforms of the SPBR in the rectifier mode (**top**) and the inverter mode (**bottom**). C_1 (dark blue) is the mains voltage V_{AC} (100 V/div), C_2 (magenta) is the mains current I_{AC} (20 A/div), C_3 (light blue) is the bridge voltage V_{ab} (100 V/div), and C_4 (brown) is the DC voltage V_{DC} (100 V/div). Time base is 5 ms/div.

A fully functional control circuit designed for unipolar operation mode was also presented that can be easily implemented in the PSIM simulator. It has made it possible to verify the correct operation of the converter and was the basis of the control finally implemented in a system based on FPGA.

The feasibility of this design has been verified with the construction and testing of a 10 kW converter using SiC MOSFET transistors, where an efficiency greater than 97% was achieved.

8. Conclusions

The power stage and control circuit of a single-phase bidirectional rectifier (SPBR) used for the bidirectional charging of electric vehicle batteries was fully designed in this study.

The working conditions of the converter have been determined by a thorough examination of its switching sequence in the rectifier and inverter operation modes.

To verify the viability of the design, a complete analysis of power losses was developed, making possible the accurate designing of parts and estimating the converter's efficiency since all power losses have been correctly calculated. All these data determined that the SPBR converter is an effective solution.

By conducting a comprehensive loss study using different types of semiconductor devices, a method has been developed that allows the selection of the optimal operating frequency, thereby maximizing converter efficiency.

The results of this study are directly applicable to the design of bidirectional input converters in electric vehicle charging applications connected to single-phase electrical grids. The bidirectional characteristic of this converter allows its use in smart grids or systems where the energy stored in electric vehicle batteries can be utilized to stabilize voltage and frequency fluctuations in the grid.

Conducting further research is planned to extend the obtained results to other SPBR converter topologies and with the selection of different magnetic components for the design of the inductance in the AC side of the converter.

Abbreviations

Acronyms

AWG	American Wire Gauge
BDC	Bidirectional DC-DC Converter
BPWM	Bipolar Pulse Width Modulation
DAB	Dual Active Bridges
DAHB	Dual Active Half-Bridges
DCR	DC Resistance
DSO	Digital Storage Oscilloscope
EMI	Electromagnetic Interference
ESR	Equivalent Series Resistance
EV	Electric Vehicle
FPGA	Field-Programmable Gate Array
GaN	Gallium Nitride
HCC	Hysteresis Current Control
HPWM	Hybrid Modulation Pulse Width Modulation
IBDC	Isolated Bidirectional DC-DC Converters
IGBT	Isolated Gate Bipolar Transistor
MOSFET	Metal-Oxide-Semiconductor Field-Effect Transistor
PF	Power Factor
PFC	Power Factor Correction
PWM	Pulse Width Modulation
Si	Silicon
SiC	Silicon Carbide
SPBR	Single-Phase Bidirectional Rectifier
SPWM	Sine Pulse Inverter Width Modulation
THD	Total Harmonic Distortion

UPWM	Unipolar Pulse Width Modulation
V2G	Vehicle-to-Grid
V2H	Vehicle-to-Home
VSI	Voltage Source Inverter

References

1. IRENA. *Smart Electrification with Renewables: Driving the Transformation of Energy Services*; International Renewable Energy Agency: Abu Dhabi, United Arab Emirates, 2022.
2. Zhou, K.; Fang, H.; Liu, Y. Driving–Charging Integrated Controller for Electric Vehicles. *IEEE Access* **2022**, *10*, 66545–66563. [CrossRef]
3. Esteve, V.; Bellido, J.L.; Jordán, J.; Dede, E.J. Improving the Efficiency of an Isolated Bidirectional Dual Active Bridge DC–DC Converter Using Variable Frequency. *Electronics* **2024**, *13*, 294. [CrossRef]
4. Monteiro, V.; Pinto, J.G.; Afonso, J.L. Operation Modes for the Electric Vehicle in Smart Grids and Smart Homes: Present and Proposed Modes. *IEEE Trans. Veh. Technol.* **2016**, *65*, 1007–1020. [CrossRef]
5. de los Mozos, A.B.; Mouli, G.R.C.; Bauer, P. Evaluation of topologies for a solar powered bidirectional electric vehicle charger. *IET Power Electron.* **2019**, *12*, 3675–3687. [CrossRef]
6. Jahnes, M.; Zhou, L.; Eull, M.; Wang, W.; Preindl, M. Design of a 22-kW Transformerless EV Charger with V2G Capabilities and Peak 99.5% Efficiency. *IEEE Trans. Ind. Electron.* **2023**, *70*, 5862–5871. [CrossRef]
7. Inoue, S.; Akagi, H. A bidirectional dc–dc converter for an energy storage system with galvanic isolation. *IEEE Trans. Power Electron.* **2007**, *22*, 2299–2306. [CrossRef]
8. Inoue, S.; Ishigaki, M.; Takahashi, A.; Sugiyama, T. Design of an Isolated Bidirectional DC–DC Converter with Built-in Filters for High Power Density. *IEEE Trans. Power Electron.* **2021**, *36*, 739–750. [CrossRef]
9. De Doncker, R.W.; Divan, D.M.; Kheraluwala, M.H. A three-phase soft-switched high-power-density DC/DC converter for high-power applications. *IEEE Trans. Ind. Appl.* **1991**, *27*, 63–73. [CrossRef]
10. Kim, H.-S.; Ryu, M.-H.; Baek, J.-W.; Jung, J.-H. High-Efficiency Isolated Bidirectional AC–DC Converter for a DC Distribution System. *IEEE Trans. Power Electron.* **2013**, *28*, 1642–1654. [CrossRef]
11. Singh, B.; Singh, B.N.; Chandra, A.; Al-Haddad, K.; Pandey, A.; Kothari, D.P. A review of single-phase improved power quality AC-DC converters. *IEEE Trans. Ind. Electron.* **2003**, *50*, 962–981. [CrossRef]
12. Kolar, J.W.; Friedli, T. The essence of three-phase PFC rectifier systems—Part I. *IEEE Trans. Power Electron.* **2013**, *28*, 176–198. [CrossRef]
13. Schrittwieser, L.; Kolar, J.W.; Soeiro, T.B. Novel SWISS Rectifier Modulation Scheme Preventing Input Current Distortions at Sector Boundaries. *IEEE Trans. Power Electron.* **2017**, *32*, 5771–5785. [CrossRef]
14. Salmon, J.; Wang, L.; Noor, N.; Krieger, A.W. A carrier-based unipolar PWM current controller that minimizes the PWM-cycle average current error using internal feedback of the PWM signals. *IEEE Trans. Power Electron.* **2007**, *22*, 1708–1718. [CrossRef]
15. Mohan, N.; Undeland, T.; Robbins, W. *Power Electronics Converters, Applications, and Design*; Wiley: New Delhi, India, 2003.
16. Li, R.T.H.; Chung, H.S.-H.; Lau, W.-H.; Zhou, B. Use of hybrid PWM and passive resonant snubber for a grid-connected CSI. *IEEE Trans. Power Electron.* **2010**, *25*, 298–309. [CrossRef]
17. Shukla, A.; Ghosh, A.; Joshi, A. Hysteresis modulation of multilevel inverters. *IEEE Trans. Power Electron.* **2011**, *26*, 1396–1409. [CrossRef]
18. Liao, Y.-H. A Novel Reduced Switching Loss Bidirectional AC/DC Converter PWM Strategy with Feedforward Control for Grid-Tied Microgrid Systems. *IEEE Trans. Power Electron.* **2014**, *29*, 1500–1513. [CrossRef]
19. Su, M.; Wu, S.; Dan, H.; Xu, J.; Sun, Y.; Wang, H.; Liu, Y.; Xiong, W.; Liang, X. A Natural Bidirectional Isolated Single-Phase AC/DC Converter with Wide Output Voltage Range for Aging Test Application in Electric Vehicle. *IEEE J. Emerg. Sel. Top. Power Electron.* **2021**, *9*, 3489–3500. [CrossRef]
20. Du, Y.; Bhat, A.K.S. Analysis and Design of a High-Frequency Isolated Dual-Tank LCL Resonant AC–DC Converter. *IEEE Trans. Ind. Appl.* **2016**, *52*, 1566–1576.
21. Wyss, J.; Biela, J. Optimal Design of Bidirectional PFC Rectifiers and Inverters Considering 2L and 3L Topologies with Si, SiC, and GaN Switches. *IEEJ J. Ind. Appl.* **2019**, *8*, 975–983. [CrossRef]
22. Biela, J.; Kolar, J.W.; Deboy, G. Optimal design of a compact 99.3% efficient single-phase PFC rectifier. In Proceedings of the 2010 Twenty-Fifth Annual IEEE Applied Power Electronics Conference and Exposition (APEC), Palm Springs, CA, USA, 21–25 February 2010; pp. 1397–1404.
23. Georgakas, K.; Safacas, A. Switching frequency determination of a bidirectional AC–DC converter to improve both power factor and efficiency. *Electr. Power Syst. Res.* **2011**, *81*, 1572–1582. [CrossRef]
24. Meng, J.; Ricco, M.; Luo, G.; Swierczynski, M.; Stroe, D.-I.; Stroe, A.-I.; Teodorescu, R. An Overview and Comparison of Online Implementable SOC Estimation Methods for Lithium-Ion Battery. *IEEE Trans. Ind. Appl.* **2018**, *54*, 1583–1591. [CrossRef]

25. Abdel-Rahman, S.; Fontana, N. *CoolSiC Totem-Pole PFC Design Guide and Power Loss Modelling*; Infineon Technologies AG: Neubiberg, Germany, 2023.
26. Esteve, V.; Jordán, J.; Dede, E.J.; Martinez, P.J.; Ferrara, K.J.; Bellido, J.L. Comparative analysis and improved design of LLC inverters for induction heating. *IET Power Electron.* **2023**, *16*, 1754–1764. [CrossRef]